Exciton Heating Versus Cooling: Charge Separation Driven by Entropy and Delocalization at Interfaces with Planar Molecules

Tika R. Kafle and Wai-Lun Chan

Phys. Rev. Applied **15**, 044054 — Published 30 April 2021

DOI: 10.1103/PhysRevApplied.15.044054

Exciton Heating versus Cooling: Charge Separation Driven by Entropy and Delocalization at Interfaces with Planar Molecules

Tika R. Kafle,* W. –L. Chan†

Department of Physics and Astronomy, University of Kansas, Lawrence, KS 66045

Abstract:

The recent development of non-fullerene acceptors (NFAs) has resulted in an abrupt increase in the organic photovoltaic (OPV) efficiency. It remains unclear why charge separation (CS) can occur at a high yield in NFA OPVs despite of the small energy level offset at the donor/acceptor (D/A) interface. In order to resolve this issue, zinc phtholacyanine (ZnPc) and its fluorinated derivative (F_8ZnPc) are used to build a model D/A interface for understanding the mechanism underlying the efficient CS in NFA OPVs. At this interface, we found that bound charge transfer (CT) excitons can undergo a heating process in which the enthalpy increases at a surprisingly fast rate. Specifically, the CT exciton gains 0.3 eV from the environment in merely 10 ps. This fast exciton heating, which eventually leads to CS, resembles the CS behavior observed in NFA bulk heterojunctions (BHJs). Interestingly, when the pair of D/A molecules switches from a face-on to an edge-on orientation, the CT exciton heating process is reversed to the typical hot CT exciton cooling process in which the enthalpy decreases with time. By using sub-bandgap excitation, we further find that the exciton heating can occur directly from cold CT excitons without the need of excess energy provided by the energy level offset. The competition between the exciton heating and cooling is explained by a model that incorporates the effect of entropy, electron delocalization and structural anisotropy. It is found that for the face-on orientation, the small contact area between the delocalized electron and hole within the CT exciton significantly reduces the number of cold CT states, which increases the entropic driving force and drives the reaction into the heating direction. This finding provides insight on why the entropy-and-delocalization driven CS would preferentially occur in NFA BHJs. The relative orientation of the NFA molecular stack and the polymer chain, together with bulky side groups, make the delocalized electron and hole in contact with each other *via* isolated point-like junctions, which is the key for activating the exciton heating and subsequent CS.

*tika.kafle@colorado.edu, †wlchan@ku.edu

I. INTRODUCTION

Because of the weak dielectric screening, electron and hole are bound together to form excitons in organic semiconductors. At an electron donor/acceptor (D/A) interface, charge transfer (CT) excitons with its electron and hole separated by the interface can be formed. These CT excitons typically have a Coulomb binding energy of 0.1 – 0.5 eV [1,2], which is much larger than the thermal energy at room temperature (25 meV). Hence, the separation of CT excitons into free carriers becomes a bottleneck step for charge generation [3-8]. In applications such as organic photovoltaics (OPVs), separating these bound excitons often results in energy loss, which in turn limits the open circuit voltage (V_{OC}) of the OPV device [9-11]. Indeed, the OPV's efficiency has plateaued at ~12% for nearly a decade since the early 2010s. The low efficiency of OPVs compared to inorganic counterparts is attributed to the larger energy loss associated with separating the bound exciton [9]. An exciting breakthrough came from the development of non-fullerene acceptors (NFAs) [12,13], which results in an abrupt increase in the efficiency of the single junction OPV from ~12% to ~17% in just ~2 years [14]. Champion single junction OPVs using NFAs has recently reached an efficiency of 18% [15-18]. Interestingly, the NFA somehow overcomes the fundamental limit on charge separation (CS) set forth by the strong exciton binding. In NFA OPVs, charges can be generated with a high yield even when the energy level offset (E_{off}) at the D/A interface is small [12,19,20]. Hence, a large V_{OC} and a high photocurrent can be attained simultaneously. Why bound CT excitons can dissociate at these polymer/NFA D/A interfaces so efficiently even for a small E_{off} at the D/A interface remains an open question.

One widely adopted mechanism on how exciton binding energy can be overcome during CS is the generation of free charges from the so-called hot CT exciton [3,4,7,8,21-23]. These hot CT excitons are spatially-delocalized and have an energy close to that of the free electron-hole pair. Hence, the whole CS process (from singlet (S_1) to free electron-hole pair) can occur on a sub-ps timescale by kinetically avoiding the lower energy, cold CT state [24-30]. However, this mechanism intrinsically requires a large E_{off} at the D/A interface because the initial S_1 exciton needs to have enough energy to access the hot CT state (Fig. 1a). Here, E_{off} is defined as the energy difference between the S_1 state in the donor and the cold/relaxed CT state. On the other hand, for the recently discovered NFA/polymer bulk heterojunctions (BHJs), because of the small E_{off}, the S_1 exciton is almost in resonance with the cold CT exciton state (Fig. 1b) [31].

Hence, hot CT states cannot be directly populated by the initial electron transfer and CS can only occur *via* cold CT states.

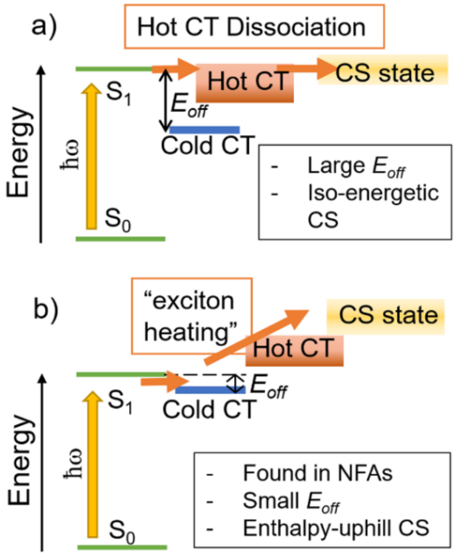

Figure 1: a) The hot CT mechanism requires a large E_{off} at the D/A interface so that the initial CT process can directly populate higher energy hot CT states. (b) The hot CT mechanism will not work at the D/A interface found in NFA BHJs. Because of the small E_{off}, the S_1 state is almost in resonance with the cold CT state. Hence, CS must occur *via* cold CT states, which is an enthalpy-uphill process.

Dissociation of cold CT excitons into free carriers is an energy (or more precisely, enthalpy) uphill process. Considering a typically CT exciton binding energy of ~ 0.1 – 0.5 eV [1,2], the CS process is slow. For example, the dissociation time for cold CT excitons in fullerene BHJs with a small E_{off} is on the order of a few ns [32,33], which is comparable to the germinate recombination time and leads to significant recombination losses. However, the observed CS time in NFA BHJs is only ~10 – 100 ps despite the small E_{off} [31,34,35], which is ~ 10 – 100 times shorter than the typical thermal dissociation time of cold CT excitons. Hence, an important question arises: why the CS in NFA BHJs can appear to be faster and has a close to 100% yield even though the CS is an enthalpy-uphill process?

Recently, we have discovered that at the ZnPc/F_8ZnPc D/A interface, an enthalpy-uphill CS process (with $\Delta E \approx 0.3$ eV) can occur spontaneously in ~10 ps after bound CT excitons is formed [36]. We will refer this spontaneous enthalpy-uphill process to as "exciton heating". This is essentially the reverse of the hot exciton cooling process commonly discussed in the literature. The characteristics of the observed CS behavior at this model interface [36] resembles many of the features observed in NFA BHJs. First, the E_{off} at the ZnPc/F_8ZnPc is relatively small [36], forcing the CS to be an enthalpy uphill process. Second, the CS process occurs on the ~ 10 ps timescale, which is similar to those found in NFA BHJs [31,34]. This moderate timescale is slower than that of the hot CT exciton dissociation (< 1 ps) [24,27], but faster than that of the classical thermal-activated mechanism (> 1 ns) [32]. Third, the CS yield is insensitive to temperature [36], which seems to disagree with the expectation of an enthalpy-uphill process, but this behavior is in accord with the CS behavior found in NFA BHJs [37]. Previously, by contrasting the CT exciton heating observed in ZnPc/F_8ZnPc to the typical hot CT exciton cooling observed in fullerene D/A interfaces [38,39], we hypothesized that the enthalpy uphill CS is driven by the combined effect of entropy and electron delocalization [36]. More importantly, the entropic driving force can be maximized by varying the relative orientation of the delocalized electron and hole within the CT exciton, which would potentially explain why the entropy-and-delocalization driven CS mechanism can be more predominant in NFA BHJs than in fullerene BHJs.

In order to pinpoint the effect originated from the wavefunction orientation, we need to keep other factors, such as the interfacial energy level alignment and the pair of molecules used to build the D/A interface, fixed while the orientation is varied. In this work, we achieve this goal by growing ZnPc/F_8ZnPc bilayer samples on different substrates. Changing the molecules from a face-on to and edge-on orientation allows us to switch the relative orientation of the delocalized electron and hole within the CT exciton. As we will show, this can significantly alter the entropy function $S(E)$ and determine whether the entropy-driven CS can be activated. Experimentally, while CT excitons can be formed on the sub-ps timescale at both interfaces, only the ZnPc/F_8ZnPc interface with a face-on orientation exhibits the aforementioned exciton heating process through which the CT exciton gains an energy of ~ 0.3 eV from the environment in ~ 10 ps. Strikingly, the ZnPc/F_8ZnPc interface with an edge-on orientation exhibits the opposite behavior, i.e. the hot CT exciton cooling. At the edge-on interface, the CT exciton loses its energy to the environment after its initial formation. Hence, the change in the orientation not merely changes a rate constant, but it also drastically *reverses* the reaction direction. We further perform the experiment with sub-bandgap photons as a way [40-42] to show that the observed CS channel can be initiated directly from cold CT excitons without the excess energy provided by the E_{off}. We found that the exciton heating process can occur even when the pump photon energy is below the optical bandgap of both ZnPc and F_8ZnPc. Because no excess energy is needed, the exciton heating can occur at D/A interfaces with a small E_{off} and would explain the highly efficient CS found at D/A interfaces with NFAs.

After estabishing the mechanism for the entropy-and-delocalization driven exciton heating process, we will discuss why this mechanism is relevant to the exceptional performance found in NFA BHJs. By using a model Hamiltonian, we find that a point-junction formed between the delocalized electron and hole within the CT exciton is a critical condition for activating this exciton heating process. Based on recent structural characterization works on NFA BHJs [43,44], we notice that these point-like junctions naturally form in NFA BHJs because a stack of planar NFA molecules can only have close contacts with the donor polymer chain at some isolated point-like junctions [43]. On the other hand, in fullerene BHJs, small clusters of fullerene molecules are often wrapped around by polymer chains [45-48], which increases the contact area between the delocalized electron and hole. This can explain why the proposed exciton heating can occur in NFA BHJs, but not in fullerene BHJs. Here, we emphasize that electron delocalization alone is not a sufficient condition to induce the exciton heating (e.g. electron delocalization is found in both fullerenes and NFAs). On top of delocalization, the electron and hole wavefunction must be oriented in such a way that it can maximize the entropic driving force.

II. EXPERIMENTAL METHODS

A. Sample preparation

The organic thin films used in this work was prepared by thermal deposition in an ultrahigh vacuum (UHV) chamber (base pressure ~ 1×10^{-9} Torr). The molecules F_8ZnPc and ZnPc were deposited either on a highly ordered pyrolytic graphite (HOPG) or a Si substrate (with a thin native oxide on top) to achieve the face-on or edge-on orientation, respectively. Before loading into the UHV chamber, the HOPG surface layer was peeled off using a scotch tape to expose a fresh clean surface whereas the Si substrate was ultrasonically cleaned with acetone and ethanol. Prior to deposition, both substrates were annealed in the UHV chamber at 400°C for ~12 hours. Then, a ZnPc layer with a nominal thickness of 10 nm was deposited on the substrate. The deposition rate, measured by a quartz crystal microbalance, was kept at 0.7 – 0.8 Å/min for the deposition on HOPG, and 2.5 – 3 Å/min for the deposition on Si (with native oxide). Previously, we found that these very slow deposition rates and the atomically clean UHV environment allow us to grow ultra-smooth and ordered films in a layer-by-layer fashion [39,49,50]. Then, a F_8ZnPc layer with various thicknesses was deposited on top of the ZnPc layer. The F_8ZnPc crystal is expected to adopt the same orientation as the underlying ZnPc crystal (known as van der Waals epitaxy) [51-53]. After deposition, the sample was transferred *in-situ* to another UHV chamber (base pressure ~ 5×10^{-11} Torr) where the photoemission spectroscopy measurement was performed.

B. Photoemission experiments

Ultraviolet photoemission spectroscopy (UPS) was used to measure the highest occupied molecular orbital (HOMO) position and the ionization potential (IP) of the sample. The UPS measurement was done with a photon energy of 21.22 eV (the He-I line) generated by a standard UV discharge lamp. The photoemission spectra were measured by a hemispherical electron analyzer (Phoibos 100, SPECS). The excited state dynamics was captured using time-resolved two photon photoemission spectroscopy (TR-TPPE). In these measurements, a pump laser pulse (1.77 eV, 25 fs) was used to create excitons in the sample. A probe laser pulse (4.68 eV, 65 fs) was used to ionize the electrons from the excitons. These beams are generated from two non-collinear parametric amplifiers (NOPA) that are pumped by a fs laser system (Light Conversion, Pharos 10W); see Ref. [54,55] for details. A TR-TPPE spectrum can capture both the energy and the population of the excited state.

III. EXPERIMENTAL RESULTS

A. Molecular Orientation and Band Alignment

Previously, we have shown that ZnPc and F_8ZnPc molecules grown on a highly oriented pyrolytic graphite (HOPG) substrate have a face-on orientation [36,56]. In order to switch the molecular orientation, ZnPc molecules are grown on a Si substrate with a thin layer of native oxide because ZnPc has an edge-on orientation on SiO_2 [57]. ZnPc was first deposited on SiO_2/Si in an ultrahigh vacuum (UHV) chamber. Then, a F_8ZnPc layer with various thicknesses was deposited on ZnPc, which is expected to have an edge-on orientation as well [58]. The desired molecular orientation can be confirmed by measuring the ionization potential (IP). It is known that the IP of phthalocyanine molecules depends on its orientation [49,59,60]. For example, the IP of CuPc, ZnPc, H_2Pc molecules with a face-on orientation is ~ 0.5 eV higher than that with an edge-on orientation. However, the opposite holds for fluorinated-Pc (e.g. F_8ZnPc) [59], i.e. the face-on orientation has a smaller IP than the edge-on orientation. This is because the H-atoms, which have a low electronegativity, on the peripheral of the planar molecule are replaced by F-atoms, which have a high electronegativity. The IP can be determined readily from the UPS spectrum by subtracting the difference between the secondary electron cut off (SECO) and the highest occupied molecular orbital (HOMO) onset from the UV photon energy (21.22 eV). The raw UPS spectra, in the energy windows near the SECO and the HOMO, are shown in Fig. S1 in the supplemental material.[61]

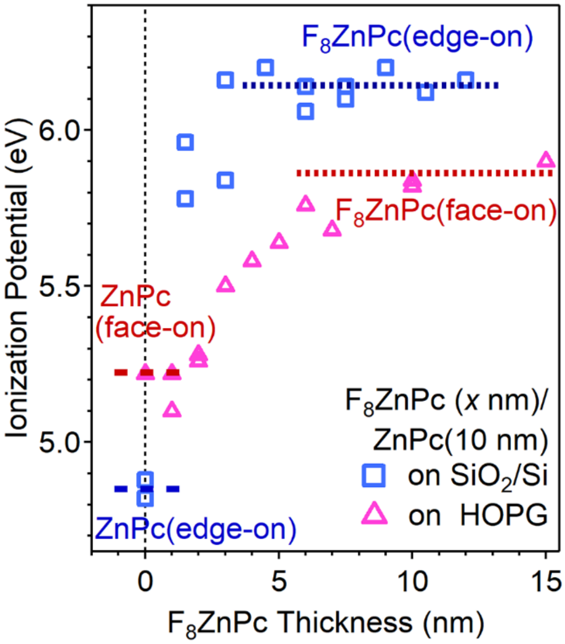

Figure 2: The IP value of the $F_8ZnPc/ZnPc$ grown on HOPG and SiO_2/Si as a function of the F_8ZnPc thickness (*x*). The ZnPc thickness is 10 nm for all samples. A zero F_8ZnPc thickness represents a bare 10-nm ZnPc film.

The IP of the $F_8ZnPc/ZnPc$ (10 nm) bilayer film grown on HOPG (red) and SiO_2/Si (blue) as a function of the F_8ZnPc thickness is shown in Fig. 2. A thickness equal to zero represents a bare 10-nm ZnPc film. For the 10-nm ZnPc film, the IP is 5.22 eV (red line) and 4.85 eV (blue line) when it is deposited on HOPG and SiO_2/Si, respectively. These values are consistent with the reported IP for ZnPc having a face-on (on HOPG) and edge-on (on SiO_2) orientations [49]. After the F_8ZnPc deposition, the IP increases because F_8ZnPc has a higher IP [58]. For thicknesses > 10 nm, the IP becomes steady and we can use this value to determine the orientation of F_8ZnPc molecules. The IP value of the 10 nm-F_8ZnPc/10 nm-ZnPc/HOPG sample is 5.86 eV while the IP value of the 10 nm-F_8ZnPc/10 nm-ZnPc/SiO_2 is 6.14 eV. These values are consistent with previous studies [62]. As discussed above, F_8ZnPc molecules with a face-on orientation should have a *smaller* IP than that with an edge-on orientation [59,63]. Hence, the F_8ZnPc molecule maintains the same orientation as the ZnPc molecule (face-on for HOPG and edge-on for SiO_2/Si) when it is deposited on ZnPc.

For the ZnPc/F_8ZnPc D/A interface, ZnPc acts as the donor while F_8ZnPc acts as the acceptor. The HOMO offset at the D/A interface can be determined from the positions of the HOMO peak in a series of UPS spectra. The HOMO position of the ZnPc relative to the Fermi level (E_f) is first determined from the spectrum of a bare 10-nm ZnPc sample. Then, the HOMO position of the F_8ZnPc relative to the E_f is determined from the F_8ZnPc/ZnPc sample. Subtracting the F_8ZnPc HOMO position from the ZnPc HOMO position allows us to determine the HOMO offset. We note that the F_8ZnPc HOMO position varies with the F_8ZnPc thickness because factors such as the local electric potential [64], the dielectric environment and the long range Coulomb interaction between ZnPc and F_8ZnPc[58] can be affected by the overlayer (F_8ZnPc) thickness. Hence, the same F_8ZnPc thickness will be chosen for both UPS and TPPE experiments when the two sets of data are compared. To select the specific F_8ZnPc thickness that we use for our experiments, we recognize that ZnPc and F_8ZnPc are planar molecules which stack as 1D columns in their crystals. For face-on samples, because the delocalized electron is oriented perpendicular to the interface along the π-stacking direction (Fig. 3a), we will focus on samples with a thicker F_8ZnPc layer (5 nm) such that the CT exciton delocalization and its dynamics will not be constrained by the sample thickness [36]. Using UPS spectra for a F_8ZnPc thickness of 2 – 5 nm, the HOMO offset is found to be ~ 0.52 eV, which will be used later to determine the energy offset between the S_1 and the CT state (E_{off} in Fig. 1). For edge-on samples, the electron and hole in the CT exciton delocalize in a direction that is parallel to the interface (Fig. 3d). Hence, CT exciton delocalization and CS is intrinsically confined in a 1D-line that is parallel to the interface. For this interface, we will focus on results obtained from the F_8ZnPc (1.5 nm)/ZnPc (10 nm) sample. Indeed, for the edge-on samples, our results show that the CT exciton is essentially confined in the layer next to the interface even for samples with a thicker F_8ZnPc layer. The HOMO offset for the edge-on orientation is ~ 0.64 eV, which is slightly larger than that of the face-on orientation.

B. CT Exciton Dynamics: Heating versus Cooling

TR-TPPE spectroscopy was used to measure the CT exciton dynamics. This method uses a pump pulse to excite the sample, and a UV pulse as the probe, which photo-emits electrons from excited states. By measuring the kinetic energy of the emitted electrons, photoemission spectroscopy probes the electronic energy of excited states directly. Previously, we have utilized this unique capability to resolve CT exciton states with different binding energies [38,39]. Moreover, it is a surface sensitive technique because of the limited escape depth (~ 1- 3 nm) [65,66] of photoelectrons. Hence, by using films with different thicknesses, we were able to obtain spatial information such as the electron delocalization size of CT excitons [38,39] and the transport of electrons or excitons across the layer [36,50,55].

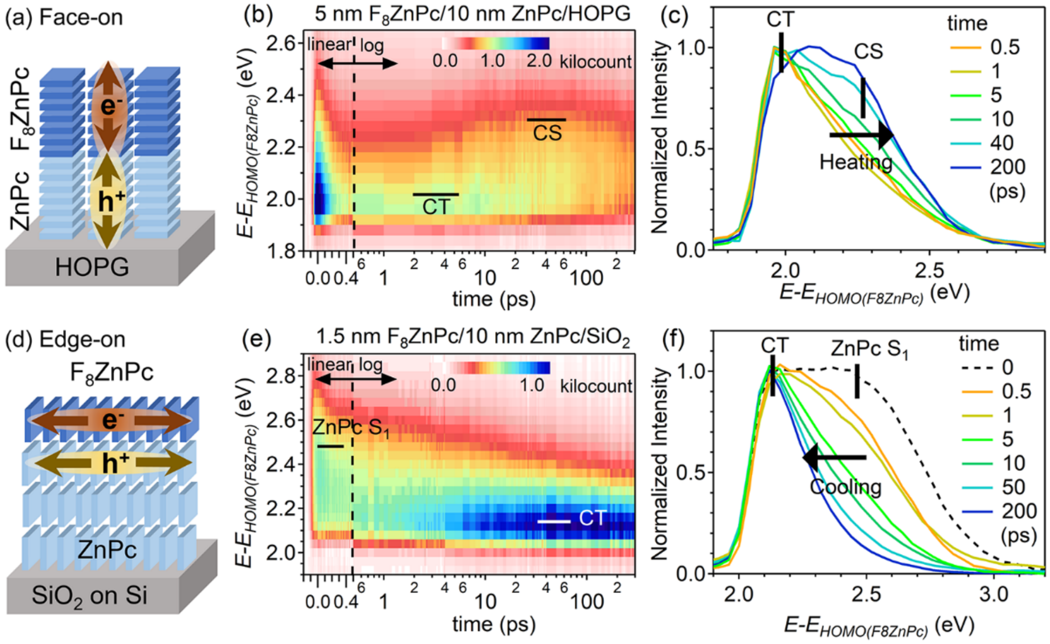

Figure 3: (a) A schematics of the F_8ZnPc/ZnPc interface with a face-on orientation. The delocalized electron and hole within the CT exciton is oriented perpendicular to the interface. (b) The TR-TPPE spectrum of the 5-nm F_8ZnPc/10-nm ZnPc/HOPG sample. On HOPG, the molecules have a face-on orientation. (c) A series of normalized spectra at various delay times, obtained from the spectrum in (b), shows that the spectral weight shifts to a higher energy as the time increases (exciton heating). (d) A schematics of the F_8ZnPc/ZnPc interface with an edge-on orientation. The delocalized electron and hole within the CT exciton is oriented parallel to the interface. (e) The TR-TPPE spectrum of the 1.5-nm F_8ZnPc/10-nm ZnPc/SiO_2/Si sample. On SiO_2, the molecules have an edge-on orientation. (f) A series of normalized spectra at various delay times, obtained from the spectrum in (e), shows that the spectral weight shifts to a lower energy as the time increases (exciton cooling).

Figure 3b shows the TR-TPPE spectrum obtained from the F_8ZnPc(5 nm)/ZnPc(10 nm) grown on the HOPG which have a face-on orientation. The pump photon energy is 1.77 eV, which matches the optical bandgap of ZnPc and F_8ZnPc (optical absorption spectra are shown in Fig. S2 in the supplemental material [61]). In the TPPE spectrum, the energy axis is referenced with respect to the F_8ZnPc's HOMO peak position obtained by the UPS. The details on how different peaks are assigned can be found in Ref. [36]. Here, we will focus on the spectral evolution for $t > 0.5$ ps. Previously, we found that for $t > 0.5$ ps, the spectrum can be roughly decomposed into a CT state and a charge separated (CS) state [36]. The CT state is located at ~

2.0 eV on the spectrum. By subtracting the HOMO offset from this energy, we can obtain a CT exciton energy of ~ 1.48 eV. A very weak shoulder at ~1.5 eV (810 nm) is also observed in the optical absorption spectrum of our bilayer sample (Fig. S2), which is consistent to the weak optical absorption of the CT state. We note that this CT exciton energy is an estimate because, as mentioned earlier, the HOMO offset measured by the UPS depends on the F_8ZnPc thickness. Nevertheless, the value we obtained agrees well with an independent study on ZnPc/F_8ZnPc blend [67], in which a CT exciton energy of ~ 1.5 eV was found by using photoluminescence spectroscopy. Because the ZnPc's S_1 energy is ~ 1.8 eV, the S_1-CT E_{off} at the D/A is ~ 0.3 eV. A peak at ~2.3 eV above the F_8ZnPc's HOMO emerges at longer delay times. This peak is assigned to the CS state because its position is close to that of the F_8ZnPc's LUMO [36]. Interestingly, the intensity of the CT state decays while the intensity of the higher energy CS state rises (Fig. 3b), which indicates the occurrence of an enthalpy-uphill CS process. We note that both the CT and CS states are not found in the spectrum of the F_8ZnPc-only sample (Fig. S3 in the supplemental material [61]). This further confirms that those two states are originated from the CT at the D/A interface.

Figure 3c shows the normalized spectra at different delay times. The maximum intensity of all spectra is normalized to one in order to compare their spectral shape. The gradual shift in the spectral weight towards the higher energy can be clearly seen. At longer delay times (e.g. 200 ps), the spectrum represents an equilibrated mixture of the CT and CS states. As TR-TPPE measures the electron energy directly, our result unambiguously demonstrates that the energy of the excited state increases by ~ 0.3 eV in a relative short period of time. Detailed analysis shows that the CS state has a rise time of ~ 15 ps [36]. Hence, the exciton heating process occurs at a rate of ~10^{11} s^{-1}, which is faster than the expected Arrhenius rate**.** For a typical attempt frequency of 10^{14} s^{-1} [68] and an energy barrier of ~ 0.2 – 0.3 eV, the Arrhenius rate is only ~10^9 s^{-1}, which is ~ 2 order of magnitudes slower. In addition to the fast reaction rate, by the principle of the detailed balance, if the enthalpy change is the only major contribution to the free energy change (i.e. if $\Delta F \sim \Delta E$), the ratio of the concentration of the higher energy CS state (n_{CS}) to that of the lower energy CT state (n_{CT}) at equilibrium should be given by $\exp(-\Delta E/k_BT)$. For ΔE ~0.2 – 0.3 eV, this ratio is ~ 10^{-4} – 10^{-6}. This low concentration of the CS state relative to the CT state should render the higher energy CS state unobservable in our experiment. Hence, the emergence of the higher energy CS state in the spectrum (both in terms of the rate and the high relative concentration) supports that the entropy contribution ($-T\Delta S$) to ΔF cannot be neglected. We note that the spectrum shown in Fig. 3b is rather atypical. For most materials that we have worked on, we find that the population of lower energy states increases at the expense of the population of higher energy states [25,38,39,55,69-71].

Previously, we hypothesize that whether the entropy-driven CT exciton heating can be activated depends on the relative orientation of the electron and hole wavefunction within the CT exciton [36]. To prove our hypothesis, we perform another set of experiments on the same F_8ZnPc/ZnPc interface, but with an edge-on orientation. Because of the van der Waals epitaxial growth [51-53], rows of F_8ZnPc molecules are expected to align in parallel with rows of ZnPc molecules as shown in Fig. 3d. The TR-TPPE spectrum for an edge-on sample is shown in Fig. 3e. In this sample, because of the thin F_8ZnPc layer (1.5 nm), the ZnPc's S_1 peak originated from the underneath ZnPc layer can also be observed. Similar to Fig. 3b, the energy scale on this spectrum is referenced with respect to the F_8ZnPc's HOMO. Subtracting the HOMO offset (0.64 eV) from the ZnPc's S_1 peak location (2.45 eV) yields 1.81 eV, which agrees well with the ZnPc's S_1 energy. A state at a lower energy position (~ 2.14 eV) emerges at $t > 1$ ps, which is assigned to the CT exciton state. Subtracting this energy by the HOMO offset (0.64 eV) yields a CT exciton energy of ~ 1.5 eV, which is consistent with the CT exciton energy found for the face-on orientation and from the optical absorption spectrum (Fig. S2). Interestingly, no CT exciton heating is observed at this interface. Instead, the intensity cascades down to lower energies with the increase in time. Therefore, CT exciton cooling instead of heating is observed at the edge-on interface. The narrowing of the spectrum towards lower energies can be seen by comparing the normalized spectra at different delay times (Fig. 3f). While some of the spectral narrowing at early times (< 5 ps) is contributed by the decay of the ZnPc's S_1 state, the spectral narrowing at longer delay times (> 5 ps) is primarily originated from the CT exciton cooling. This is because, as we will show, similar narrowing can be observed in samples with a thicker F_8ZnPc overlayer in which the ZnPc's S_1 state can no longer be observed.

In order to show that the absence of exciton heating is not because of the artificial confinement introduced by the ultrathin F_8ZnPc layer, we also perform experiments with a thicker F_8ZnPc layer. Figure 4a shows the TR-TPPE spectrum of the F_8ZnPc (4.5 nm)/ZnPc (10 nm) sample. A CT state (for $t > 1$ ps) with its dynamics similar to that of the 1.5 nm sample is found (Fig. 4d), but the TPPE intensity is ~ 10 times weaker. The weaker intensity can be explained by the fact that the delocalized electron within the CT exciton is located in the layer next to the D/A interface at an edge-on interface (Fig. 3d). Because photoemission is a surface sensitive probe, a thicker F_8ZnPc overlayer causes a rapid diminishing of the photoemission intensity originated from the CT exciton residing close to the interface. Moreover, in this thicker sample, because the ZnPc layer is fully covered by the thicker 4.5-nm F_8ZnPc layer, the signal from the ZnPc's S_1 peak is too weak to be observed. Figure 4b shows the normalized spectra at different delay times. The aforementioned spectral narrowing can still be observed, but to a lesser extent. Due to the disappearance of the ZnPc's S_1 signal, we attribute this spectral narrowing to the CT exciton cooling. For an even thicker F_8ZnPc layer (e.g. 12.5 nm), the CT state is no longer observed. The spectrum of the 12.5 nm sample is shown in the supplemental material (Fig. S4) [61]. The TPPE intensity for these thick samples is weak because the F_8ZnPc's S_1 level is outside the spectral range accessible by the 4.68 eV probe photon [36]. Moreover, the intensity decays monotonically (dashed line in Fig. 4d), which has a shorter lifetime compared to that of the CT state but is similar to the S_1 lifetime in a bare ZnPc film [39,55,72].

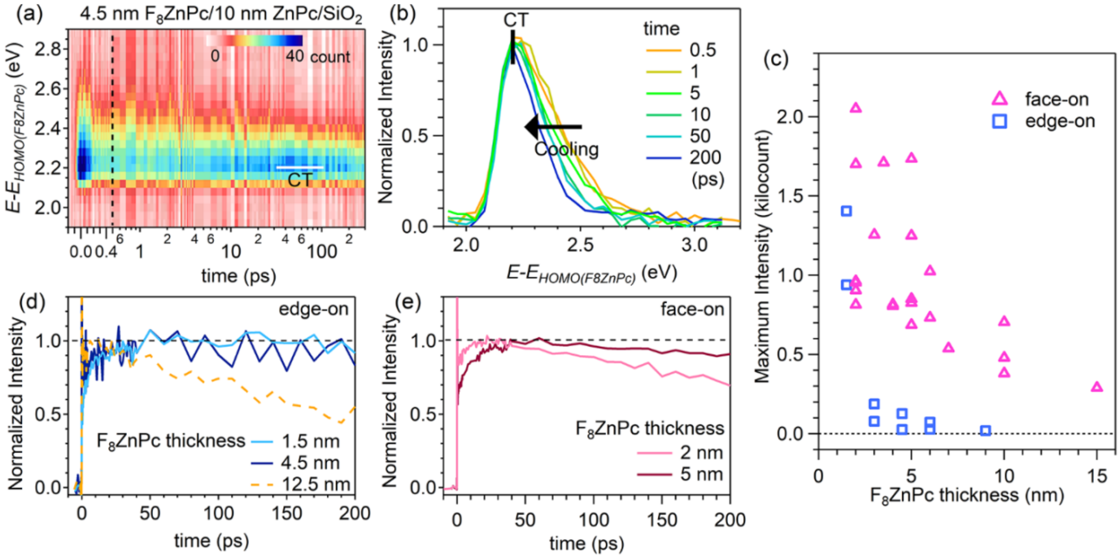

Figure 4: (a) The TR-TPPE spectrum of the 4.5-nm F_8ZnPc/10-nm ZnPc/SiO_2/Si sample. The spectrum is similar to the one shown in Fig. 3e except that the ZnPc's S_1 state cannot be observed because of the thicker F_8ZnPc overlayer. (b) A series of normalized spectra at various delay times, obtained from the spectrum in (a). (c) The signal intensity for the CT/CS state as a function of the F_8ZnPc thickness. For the edge-on orientation, the intensity decays much more rapidly with the thickness because the electron in the CT exciton is confined in the F_8ZnPc layer right next to the interface. (d) For the edge-on orientation, the 4.5-nm and 1.5-nm F_8ZnPc samples show similar CT exciton dynamics. (e) For the face-on orientation, the 5-nm and 2-nm F_8ZnPc samples show different exciton dynamics because the separated electron is spreading towards the sample surface.

Figure 4c compares the intensity of the CS state and the CT state, as a function of the F_8ZnPc thickness, for the face-on and edge-on orientation, respectively. The intensity is chosen at the delay time at which the intensity reaches the maximum. Because photoemission mainly probes the sample surface, the intensity roughly represents how far the delocalized electron spreads away from the interface convoluted by the escape depth of photoelectrons (~1 – 3 nm) [65,66]. As expected, the signal intensity decays slower for the face-on orientation because the delocalized electron is orientated perpendicular to the D/A interface. On the contrary, for the edge-on orientation, the delocalized electron is confined within the layer that is next to the interface, which causes the intensity to drop rapidly as a function of the F_8ZnPc thickness. The orientation of the delocalized electron also manifests in the dynamics. Figure 4d compares the CT exciton dynamics for the 1.5-nm and 4.5-nm F_8ZnPc samples with an edge-on orientation. The CT dynamics for the two samples is essentially the same because the electron is confined in the layer that is right next to the interface. Hence, a thicker F_8ZnPc layer is not expected to change the CT exciton dynamics. By contrast, for the face-on orientation (Fig. 4e), the dynamics depends on the thickness. In particular, the time at which the CS signal reaches its maximum is delayed in the thicker sample. Previously, we have attributed this time delay to the time needed for separated electrons to reach the sample surface [36]. Indeed, this time increases with the F_8ZnPc thickness.

Our orientation dependent study shows that distinctly different excitonic processes are found at these two orientations. An increase in the CT exciton energy (exciton heating) is observed for the face-on orientation. By contrast, the typical CT exciton cooling is observed in samples with an edge-on orientation. We can quantify the heating/cooling by calculating the centroid $\bar{E}(t)$ of spectra shown in Fig. 3c and 3f. The $\bar{E}(t)$ is defined by Eq. (1), where $I(E)$ and E are the intensity and the energy, respectively.

$$\bar{E}(t) = \frac{\sum I(E)\times E}{\sum I(E)} \qquad (1)$$

The centroid as a function of time for the two samples are shown in Fig. 5. On this plot, the energy is subtracted by the respective HOMO offsets such that the energy axis represents the average energy of the electron-hole pair (either in the form of a CT exciton or a pair of separated charges). Both the cooling and heating appear to occur on the same timescale (~ 10 ps). As we will discuss later, although we simply label the spectrum with a single CT and CS states, the spectrum should represent a manifold of CT/CS states with different delocalization sizes and energies. Hence, the heating/cooling times represent how fast different CT/CS states equilibrate, which depends on the rate at which the electron-hole pair exchanges its energy with the environment.

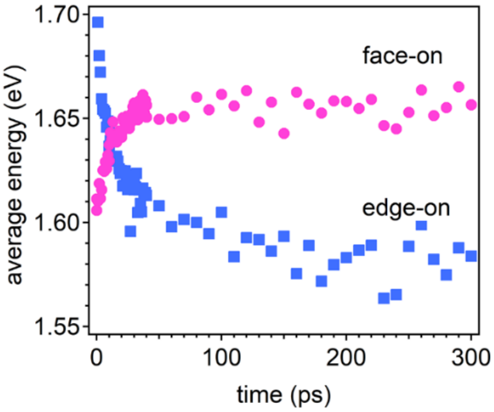

Figure 5: The evolution of the average energy of the electron-hole pair as a function of time determined from the centroid of the spectra shown in Fig. 3(c) and 3(f).

We note that, geometrically, the CT exciton found in the edge-on orientation can still be separated even though its electron and hole are spatially confined to the layer next to the interface. For instance, the electron and hole can move in opposite directions in the 1D-stack for CS to occur. Hence, the edge-on orientation itself does not preclude the occurrence of the exciton heating and the subsequent CS. Moreover, we argue that a high electron mobility cannot explain the opposite heating/cooling behavior observed for the face-on/edge-on orientations. For both orientations, the mobility is high along the π-stacking direction despite those stacking directions orientate differently in the two cases. Hence, if the high mobility can promote CS in the face-on case, it would promote CS in the edge-on case as well so far as the electron and hole can move in the opposite direction. The edge-on orientation does not prohibit such motion. Indeed, if the motion of the electron and hole are stochastic, there is a 50% chance for the electron and hole to move in the opposite direction for the edge-on orientation. Therefore, the edge-on orientation would have a slower CS rate as compared to the face-on orientation, but the CS is not particularly prohibited at the edge-on interface as compared to the face-on interface based on the anisotropy in mobility. However, as we will show, the change in the relative orientation between the delocalized electron and hole within the CT exciton significantly alters the density of states (DOS) of tightly bound CT states relative to that of loosely bound ones. This in turn changes the entropy function $S(E)$ and governs whether the entropy-driven exciton heating can occur.

C. Sub-bandgap Excitation

One of the important questions regarding the CT exciton heating process is whether it can be triggered in the absence of the excess energy provided by the S_1-CT energy offset (E_{off}). It is often thought that the E_{off} provides excess energy to drive the CS process. However, if the exciton heating is driven by the entropy, it can occur as long as the entropic driving force can compensate the enthalpy change regardless whether the cold or the hot CT state is initially populated. This property has an important consequence, i.e., the proposed mechanism can induce effective CS even at a D/A interface with a very small E_{off} (Fig. 1b). To find whether this property is possessed by the observed exciton heating process, we conduct the TR-TPPE experiment on the face-on sample, F_8ZnPc(5 nm)/ZnPc(10 nm)/HOPG, with different pump-photon energies. Pump-photon energies in the range of 1.77 eV to 1.49 eV were used. The spectra of our pump pulses centered at various wavelength are shown in Fig. S5 in the supplemental material [61]. The S_1 absorption peak of ZnPc and F_8ZnPc is at 1.8 eV and the CT exciton state has an energy of 1.5 eV. Hence, we can primarily excite the S_1 exciton and the CT exciton at the upper-end and the low-end of this photon energy range, respectively.

Figure 6a shows the TR-TPPE spectrum of the F_8ZnPc (5 nm)/ZnPc (10 nm)/HOPG sample pumped by 1.59 eV (780 nm) pulses. The CT exciton dynamics is qualitatively similar to those collected by a 1.78 eV (700 nm) pump beam (Fig. 3b) except that the signal intensity for the whole spectrum is weaker proportionately because of the much reduced optical absorption. Notably, the exciton heating is still observed with the lower pump photon energy of 1.59 eV. This photon energy is below the S_1 energy (Fig. S2) of both ZnPc and F_8ZnPc. At this photon energy, most of the excitations are created *via* the direct optical excitation of cold CT excitons. Hence, the CT exciton heating process can occur even in the absence of the excess energy provided by the S_1-CT offset. Figure 6b compares the spectra at 300 ps for different pump wavelengths. All these normalized spectra have the same shape. These spectra represent a mixture of CT and CS states. At this long delay time, an equilibrium between the CT and CS states has reached. This result shows that the system arrives at the same equilibrium state independent of the initial excitation energy.

While the same final state is reached at long delay times, the pathway taken by the system to reach this equilibrium state depends on the pump photon energy. Figure 6c shows the temporal evolution of the peak centroid $\bar{E}(t)$ for different pump wavelengths. Solid lines are the moving average of the raw data. As the pump wavelength increases, the $\bar{E}(t)$ takes a longer time to reach the final equilibrium value. Moreover, the $\bar{E}(t)$ at early times is smaller for the smaller pump photon energy. This is consistent with the expectation that more localized CT states are excited when the pump photon energy is below the S_1 energy. At the longest wavelength (830 nm) used, despite the CT state is directly populated by the pump beam (instead of populated by the charge transfer from the S_1 state), the CT exciton heating process can still occur beside at a slower rate. The slower rate would be explained by the sparse energy distribution of bound CT states. As we will show, for the face-on orientation, only a few tightly bound CT states are presence. The transition from one bound CT state to another would require overcoming some small energy gaps, which can increase the equilibration time between different CT states. Nevertheless, the result shows that the exciton heating can potentially occur at D/A interfaces with a very small E_{off} because excess energy is not required for triggering the process.

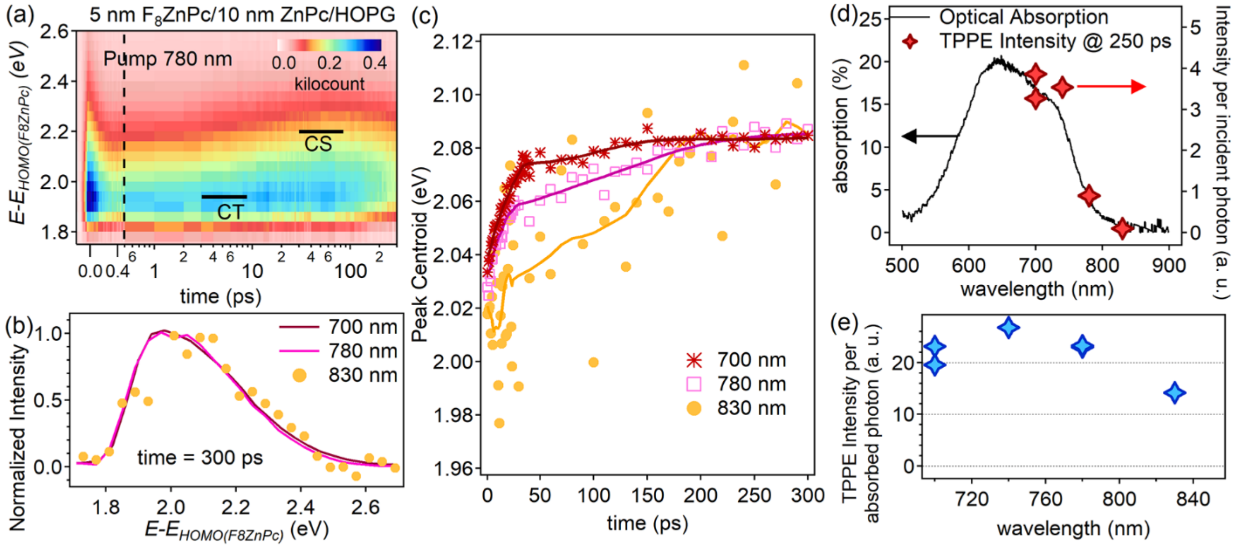

Figure 6: (a) The TR-TPPE spectrum of the 5-nm F_8ZnPc/10-nm ZnPc/HOPG sample pumped by 780 nm pulses. Exciton heating can be observed even with a sub-bandgap excitation. (b) The normalized spectra at 300 ps for experiments done with different pump wavelengths. The same spectral shape indicates that the system arrives at the same final state despite the difference in the pump photon energy (c) The centroid of the peak as a function of time for different pump wavelengths. Solid lines are the moving average of the data. As the pump-photon energy decreases, the system takes a longer time to equilibrate. (d) A comparison between the optical absorption of a F_8ZnPc/ZnPc sample (left axis) and the integrated TPPE intensity at 250 ps (right axis). (e) The TPPE intensity divided by the optical absorption at different wavelengths, which is proportional to the yield of generating the CT/CS mixture.

We also note that the integrated intensity of the TPPE spectrum at long delay times traces well with the optical absorption of the bilayer sample. The integrated TPPE intensity at t = 250 ps, normalized by the pump photon energy, is plotted together with the optical absorption spectrum in Fig. 6d. The two almost overlap with each other. Note that in this plot, we normalize the TPPE intensity with the number of incident photons (instead of the incident laser power) as the TPPE intensity is proportional to number of emitted electrons. Because the optical absorption represents the percentage of absorbed photons, the ratio of the two quantities (TPPE intensity and percentage absorption) is proportional to the number of electron-hole pairs generated per absorbed photon. This ratio is shown in Fig. 6e. Notably, from 700 nm to 780 nm, the yield for generating the CT/CS mixture does not show any decrease as the wavelength increases. At 780 nm, the pump-photon energy is already below the S_1 energy. At 830 nm, the ratio is decreased by ~ 35 % as compared to the ratio at 700 nm, which can be attributed to the longer exciton heating time observed in Fig. 6c. A longer exciton heating time allows more CT excitons to recombine before CS can occur.

IV. MODELING OF THE ENTROPIC DRIVING FORCE

Although the entropy driving force can induce the enthalpy-uphill exciton heating observed in our experiment, a major question remains; i.e. why the exciton heating can occur at the F_8ZnPc/ZnPc interface with a face-on orientation but not at the same interface with an edge-on orientation? As we will show, an answer to this question will provide important insights on why the entropy-and-delocalization driven exciton heating can occur preferentially in NFA BHJs as compared to fullerene BHJs. Existing entropy models [4,73-76] cannot answer the above question because of two deficiencies. First, most entropy models treat electron as a localized particle residing on a single molecule. Hence, the number of configurations $\Omega(E)$ is determined by merely counting the number of molecules within a certain volume. This counting method is clearly insufficient when the electron and hole within the CT exciton are spatially delocalized. Second, most models do not include the structural anisotropy commonly found in organic crystals and π-conjugated polymers. The geometric constraint imposed by the anisotropy can make the exciton binding energy highly depending on the relative orientation and the separation between the electron and the hole wavefunctions. This in turn changes the number of available CT states as a function of energy, i.e. $\Omega(E)$ and, hence, the entropy function $S(E)$.

Here, a simple tight-binding Hamiltonian was used to determine effects of crystal anisotropy and electron delocalization on the density of state (DOS) of the manifold of CT/CS states [36]. Similar tight-binding Hamiltonians have been used by others [2,77,78] to model CT excitons. In this model, the CT exciton, under the site representation, is described by a two-body wavefunction: $|i,j\rangle$. The indexes i and j represent the molecular site in the acceptor and donor crystals, respectively. For acceptor and donor crystals having N and M sites, the total number of states is $N \times M$. The Hamiltonian H for the CT states can then be written as:

$$H = \sum_{i}^{N} \sum_{j}^{M} V_c(i,j)|i,j\rangle\langle i,j| + \sum_{j}^{M} \sum_{i,n,i\neq n}^{N} J_{el}(n,i)\,|n,j\rangle\langle i,j| + \sum_{i}^{N} \sum_{j,m,j\neq m}^{M} J_h(m,j)\,|i,m\rangle\langle i,j|$$

(2)

In this Hamiltonian, $J_{el}(n, i)$ is the electron transfer integral between site n and site i in the acceptor crystal and $J_h(m, j)$ is the hole transfer integral between site m and site j in the donor crystal. We only consider the electronic coupling between the nearest neighbor sites that are along the π–stacking direction. The potential $V_c(i, j)$ represents the Coulomb interaction between electron and hole, which is given by $V_c(i,j) = -\frac{e^2}{4\pi\kappa\epsilon_0}\frac{1}{r_{i,j}}$, where ϵ_0 is the vacuum permittivity, κ is the dielectric constant, and $r_{i,j}$ is the distance between site i and site j. A dielectric constant equal to 3.5 was used, which is a typical value for organic semiconductors.

We simulate the DOS function of the CT/CS states for two rows of ZnPc(donor) and F_8ZnPc(acceptor) molecules with three different orientations (Fig. 7a). Each row of molecules is 10-nm long. The π-stacking direction, along which the electron/hole delocalizes, is indicated by orange arrows. The electron and hole transfer integral (J_{el}, J_h) between nearest neighbors was set to be 50 meV. This value is in line with typical values reported for phthalocyanine crystals [79-82]. A single value was used so that the effect from the orientation can be studied. For the crystal structure, ZnPc and F_8ZnPc were modelled by a row of molecules with intermolecular spacing equal to 0.38 nm [83] and 0.48 nm [81], respectively. For the face-on orientation, an average distance of 0.43 nm was used for the distance between ZnPc and F_8ZnPc molecules at the interface. For the edge-on orientation, the distance between ZnPc and F_8ZnPc molecules at the interface was set at 1.3 nm [83].

The energies of all the eigenstates can then be determined by diagonalizing the Hamiltonian. An eigenstate with an index k can be expressed as

$$\Psi_k = \sum_{i,j} a_{i,j}(k)|i,j\rangle, \tag{3}$$

where $a_{i,j}(k)$ is the complex amplitude of $|i,j\rangle$. Because $|i,j\rangle$ represents the electron and hole locate in the site i in the acceptor crystal and site j in the donor crystal, respectively, the electron-hole separation $r_{i,j}$ of $|i, j\rangle$ can be determined readily under this site representation by finding the distance between sites i and j. Then, the average electron-hole distance r_k for the eigenstate ψ_k is determined by

$$r_k = \sum_{i,j} \left|a_{i,j}(k)\right|^2 r_{i,j}. \tag{4}$$

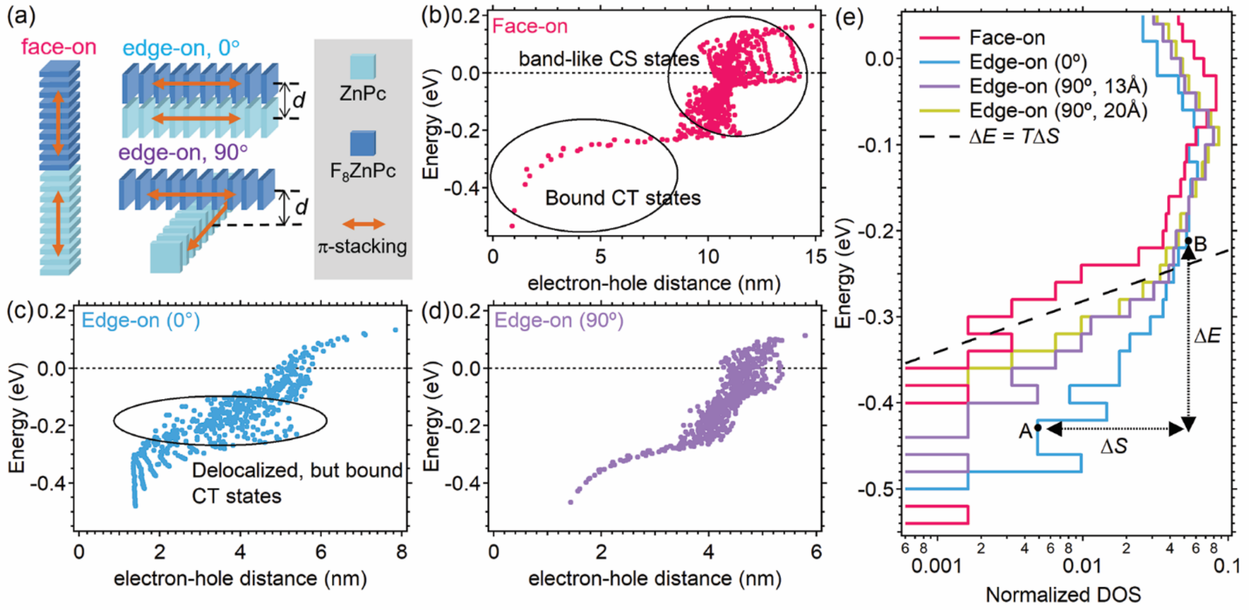

Figure 7: (a) Schematics showing the relative orientation of the rows of ZnPc and F$_8$ZnPc molecules for the 3 configurations used in our simulation. The orange arrows indicate the π-stacking direction. (b-d) The relationship between the eigenenergy and the average electron-hole distance for the 3 configurations shown in (a) determined by using the tight-binding model. Each dot represents an eigenstate. (e) The DOS functions for different configurations. The dashed-line represents the critical slope at which $T\Delta S = \Delta E$ (at room temperature).

Figure 7b shows the energies and the electron-hole distances of all eigenstates (each dot represents an eigenstate) for the interface with a face-on orientation. These eigenstates can roughly be categorized into two groups. First, those states with smaller energies (< 0.2 eV) represent bound CT states. As expected, the exciton binding energy (roughly equal to the negative of the eigenenergy) increases with a decrease in the electron-hole separation. Second, those states from -0.2 eV to 0.2 eV represent band-like CS states. Electron/hole in these states are delocalized along the whole molecular chain. Because of the delocalization, the electron-hole separation is large and the effect of the Coulomb attraction on the eigenenergy is small. Figure 7c shows the result obtained from the edge-on orientation. For the "edge-on, 0°" configuration, the two groups of states mentioned earlier merge together. This behavior can be explained by the geometric constraint imposed by the molecular orientation. Unlike the face-on orientation, the electron and hole are in close proximity with each other even if both of them are delocalized (Fig. 7a) because the two molecular rows are in parallel. As a result, energies of the majority of band-like states are lowered by the Coulomb attraction. Hence, the number of bound CT states is largely increased. In addition to the typical "face-on" and "edge-on" orientation, we also simulate the "edge-on, 90°" configuration. In this orientation, one of the molecular rows is rotated by 90° to minimize the contact area between the delocalized electron and hole. The distribution of eigenstates for this configuration is shown in Fig. 7d. By minimizing the contact area, the distribution of eigenstates restores to a distribution that is similar to that of the face-on orientation (Fig. 7b).

By counting the number of eigenstates as a function of energy *E*, we can determine the function DOS(*E*). The DOS represents the number of available states per unit energy, which is essentially the number of configurations Ω(*E*) in the equilibrium entropy function *S*(*E*). Hence, the entropy change (Δ*S*) for an incremental increase in enthalpy (Δ*E*) can be written as:

$$\Delta S(E) = S(E+\Delta E) - S(E) = k_B \ln\left(\frac{\mathrm{DOS}(E+\Delta E)}{\mathrm{DOS}(E)}\right) \ . \tag{5}$$

The DOS function for the three orientations can be determined from the distributions shown in Fig. 7b – 7d. The results are plotted in Fig. 7e. In this plot, the *x*-axis, which represents the DOS, is shown in a log scale. Hence, the horizontal distance between two points on this plot is proportional to the Δ*S* (see Eq. (5)). Likewise, the vertical distance between two points is equivalent to Δ*E*. The Δ*S* and Δ*E* during the CS process can be found on the DOS curve by finding the horizontal and vertical distances between two points that correspond to bound CT states and CS states (e.g. point A and B on Fig. 7e). A smaller slope represents a larger Δ*S* for a given Δ*E*, and, hence, a stronger entropic driving force. For reference, the black dashed line indicates the critical slope at which $T\Delta S = \Delta E$ (i.e. $\Delta F = \Delta E - T\Delta S = 0$) at room temperature. The face-on orientation (red) has a much flatter DOS curve as compared to the edge-on (0°) orientation (blue), implying that the face-on orientation has a larger entropic driving force. For the face-on orientation, because Δ*E* can be mostly compensated by *T*Δ*S* (the face-on curve has a slope similar to that of the dashed line), the CS process is essentially "barrierless". This agrees with our experimental observation, i.e. the CT exciton heating occurs spontaneously after the bound CT exciton is formed. On the other hand, the slope of the DOS is much steeper for the edge-on (0°) orientation. In this case, $T\Delta S$ is not enough to compensate ΔE and exciton cooling is preferred. Physically, for the edge-on orientation, both the hole and the electron locate very close to the interface despite delocalization, which significantly increases the number of low energy CT states and reduces the entropic driving force. On the other hand, for the face-on orientation, delocalization pushes both electron and hole away from the interface because the two rows of molecules only in contact at a single point. This increases the number of loosely-bound CT states relative to the number of tightly-bound ones, which increases the entropic driving force.

For the edge-on orientation, if we rotate one of molecular rows by 90°, the contact area between the delocalized electron and hole within the CT exciton is significantly reduced. As a result, the DOS curve is flattened (the purple curve vs the blue curve) and the entropic driving force is enhanced. The slope of the purple curve (edge-on, 90°) is similar to that of the red curve (face-on). Hence, similar to the face-on orientation, exciton heating is expected to occur. The entropy-and-delocalization driven exciton heating can be activated by reducing the contact area between the delocalized electron and hole within the CT exciton. As we will discuss, this condition is likely to fulfill in NFA BHJs where NFA stacks and donor-polymer chains can only be in contact with each other at some isolated point junctions. As a result, D/A interfaces found in NFA BHJs would favor the exciton heating process.

V. DISCUSSION

Although our work is done on a simplified model system, it is worthwhile to assess whether the proposed mechanism can potentially explain the high CS efficiency found in NFA BHJs. Recently, it has been demonstrated that a planar small molecule NFA named Y6 and its derivates can produce OPVs with an efficiency up to 18% [15-18]. Detailed structural characterizations of the champion Y6/polymer BHJs have been reported [18,43,44]. Common findings from these studies include: 1) The planar Y6 molecules stack on top of each other along the surface normal direction. The small spacing (~ 3.5 Å) between Y6 molecules results in a strong nearest-neighbor coupling and promote electron delocalization; 2) polymer chains lie parallel to the substrate (note that the hole primarily delocalizes along the polymer chain). As a result, it is likely that the delocalized electron and hole wavefunctions in a CT exciton will look like two 1D strings oriented at different directions – mostly orthogonal with each other as illustrated in Fig. 8a. This electron-hole orientation limits the spatial contact between the two wavefunctions to some isolated “hot spots” where they intersect [43] (the yellow spot in Fig. 8a).

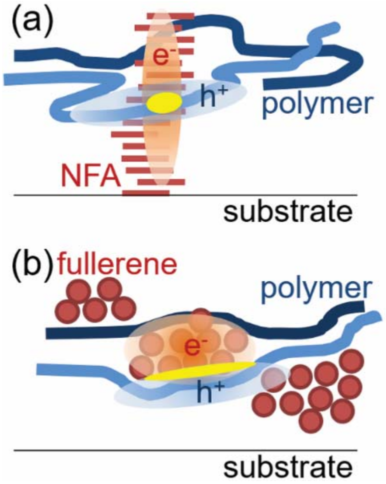

Figure 8: Schematics showing the likely microstructures of (a) NFA BHJs and (b) fullerene BHJs. Based on previous structural characterization works, it is likely that in NFA BHJs, the D/A domains intersect each other at some point-like junctions (yellow spots). On the other hand, the delocalized electron and hole have a more extended contact area in fullerene BHJs.

These isolated hot spots are quite similar to the point contact between the ZnPc and F_8ZnPc rows in the edge-on (90^o) configuration as discussed earlier. As we have already shown, the small contact area increases the entropic driving force. Furthermore, we note that in typical NFA BHJs, the distance between the delocalized electron and hole in the CT exciton is even larger because both the NFA and polymer contain some bulky side groups. For example, in the Y6 BHJs, the distance between the donor and acceptor domains at the closest contact point is ~ 20 Å [43]. If we increase the distance between the ZnPc and F_8ZnPc rows in our edge-on (90^o) configuration from the original 13 Å to 20 Å, the DOS curve is further flattened (the yellow curve in Fig. 7e). This illustrates that the increased spatial separation between the donor and acceptor domains can further increase the entropic driving force. Hence, D/A interfaces found in NFA BHJs would favor the exciton heating process, which can potentially result in effective CS even at interfaces with a small E_{off}.

On the other hand, the structure of the fullerene/polymer BHJ is quite different. It is known that CS occurs in D/A inter-mixed regions where fullerene clusters are intercalated between polymer chains [45-48]. Because of the large aspect ratio of the polymer chain, one can expect that the polymer chain wraps around nano-sized, isotropic fullerene domains in these inter-mixed regions (Fig. 8b). As a result, the contact between the electron and hole wavefunctions resembles a 1D line. This significantly increases the contact area between the delocalized electron and hole wavefunctions in the CT exciton. In some aspect, this orientation is similar to that of the ZnPc/C_{60} interface that we studied earlier. For the ZnPc/C_{60}, hot CT excitons are found to cool down to lower energy CT excitons in a few ps [38,39]. Hence, in contrast to NFA BHJs, D/A interfaces found in typical fullerene BHJs would not favor the exciton heating process.

VI. CONCLUSION

In summary, we have observed enthalpy-uphill CS *via* a CT exciton heating process at the model ZnPc/F_8ZnPc interface. The observed CS behaviors resembles many of those CS behaviors found in NFA BHJs. In particular, the enthalpy-uphill CS can occur in ~ 10 ps, which is much faster than the expected Arrhenius rate. This fast rate can outcompete CT exciton recombination. Hence, the CS can have a high yield despite it is an enthalpy uphill process. In this work, we further demonstrate that the exciton heating can only occur at the ZnPc/F_8ZnPc interface with a face-on orientation. Strikingly, by switching the molecules to an edge-on orientation, we found that the reverse process, i.e. the CT exciton cooling, occurs. Therefore, the exciton heating process can only be activated at interfaces with a proper molecular orientation. Moreover, we found that, for the face-on orientation, the exciton heating can occur even when the sample is excited by sub-bandgap photons. At the lowest photon energy used, the bound CT exciton, instead of the S_1 exciton, is optically excited. Therefore, our result shows that the exciton heating does not require the excess energy provided by the S_1-CT energy offset. Hence, it can occur at D/A interfaces with a small E_{off}.

We further show that the observed exciton heating process is driven by entropy and electron delocalization. By modeling the DOS function of the manifold of CT/CS states with a model tight-binding Hamiltonian, we find that the entropic driving force can be maximized by minimizing the contact area between the delocalized electron and hole within the CT exciton. For the face-on orientation, rows of ZnPc and F_8ZnPc only in contact with each other at a point junction. On the other hand, the two rows of molecules are fully in contact with each other for the edge-on orientation. For the face-on orientation, the small contact area, together with the delocalization, pushes the electron and hole away from each other, which significantly lowers the number of tightly bound (or cold) CT states relative to those loosely bound (or hot) ones. This in turn increases the entropic driving force and favors the exciton heating process. This argument can be potentially used to explain why entropy-and-delocalization driven CS would occur more readily in NFA BHJs as compared to fullerene BHJs. In NFA BHJs, a stack of the planar NFAs can only in contact with the donor polymer chain at some isolated point contacts. By contrast, polymer chains can wrap around fullerene clusters in fullerene BHJs, which can significantly increase the contact area between the delocalized electron and hole. The minimal contact area between the delocalized electron and hole within CT excitons found in NFA BHJs allows the entropy-and-delocalization driven CS to occur. This enables efficient CS despite of the small energy offset at the D/A interface.

Finally, we note that the exciton heating process makes the recombination of electron-hole pairs becomes unfavorable because the free energy of the system, which includes the entropic contribution, will increase when a free electron-hole pair is converted back to a bound CT exciton. This essentially makes free electrons and holes “repel” each other. Hence, the entropic driving force can also reduce non-radiative recombination and its associated energy loss. Indeed, non-radiative recombination is a major energy loss channel in OPVs but appears to be suppressed in NFA OPVs compared to fullerene OPVs [84].

ACKNOWLEDGEMENTS

The work is supported by the U. S. National Science Foundation, Grant DMR-1351716.

REFERENCES

[1] X. Y. Zhu, N. R. Monahan, Z. Z. Gong, H. M. Zhu, K. W. Williams, and C. A. Nelson, Charge Transfer Excitons at van der Waals Interfaces, J. Am. Chem. Soc. **137**, 8313 (2015).

[2] G. D'Avino, L. Muccioli, Y. Olivier, and D. Beljonne, Charge Separation and Recombination at Polymer-Fullerene Heterojunctions: Delocalization and Hybridization Effects, J. Phys. Chem. Lett. **7**, 536 (2016).

[3] J. L. Bredas, J. E. Norton, J. Cornil, and V. Coropceanu, Molecular Understanding of Organic Solar Cells: The Challenges, Acc. Chem. Res. **42**, 1691 (2009).

[4] T. M. Clarke and J. R. Durrant, Charge Photogeneration in Organic Solar Cells, Chem. Rev. **110**, 6736 (2010).

[5] A. J. Heeger, 25th Anniversary Article: Bulk Heterojunction Solar Cells: Understanding the Mechanism of Operation, Adv. Mater. **26**, 10 (2014).

[6] B. M. Savoie, N. E. Jackson, L. X. Chen, T. J. Marks, and M. A. Ratner, Mesoscopic Features of Charge Generation in Organic Semiconductors, Acc. Chem. Res. **47**, 3385 (2014).

[7] O. Ostroverkhova, Organic Optoelectronic Materials: Mechanisms and Applications, Chem. Rev. **116**, 13279 (2016).

[8] C. S. Ponseca, P. Chabera, J. Uhlig, P. Persson, and V. Sundstrom, Ultrafast Electron Dynamics in Solar Energy Conversion, Chem. Rev. **117**, 10940 (2017).

[9] J. Z. Yao, T. Kirchartz, M. S. Vezie, M. A. Faist, W. Gong, Z. C. He, H. B. Wu, J. Troughton, T. Watson, D. Bryant, and J. Nelson, Quantifying Losses in Open-Circuit Voltage in Solution-Processable Solar Cells, Phys. Rev. Appl. **4**, 014020 (2015).

[10] B. P. Rand, D. P. Burk, and S. R. Forrest, Offset energies at organic semiconductor heterojunctions and their influence on the open-circuit voltage of thin-film solar cells, Phys. Rev. B **75**, 115327 (2007).
[11] X. Liu, B. P. Rand, and S. R. Forrest, Engineering Charge-Transfer States for Efficient, Low-Energy-Loss Organic Photovoltaics, Trends in Chemistry **1**, 815 (2019).
[12] P. Cheng, G. Li, X. W. Zhan, and Y. Yang, Next-generation organic photovoltaics based on non-fullerene acceptors, Nat. Photon. **12**, 131 (2018).
[13] C. B. Nielsen, S. Holliday, H. Y. Chen, S. J. Cryer, and I. McCulloch, Non-Fullerene Electron Acceptors for Use in Organic Solar Cells, Acc. Chem. Res. **48**, 2803 (2015).
[14] NREL, Research Cell Record and Efficiency Chart, https://www.nrel.gov/pv/cell-efficiency.html.
[15] J. Yuan, Y. Q. Zhang, L. Y. Zhou, G. C. Zhang, H. L. Yip, T. K. Lau, X. H. Lu, C. Zhu, H. J. Peng, P. A. Johnson, M. Leclerc, Y. Cao, J. Ulanski, Y. F. Li, and Y. P. Zou, Single-Junction Organic Solar Cell with over 15% Efficiency Using Fused-Ring Acceptor with Electron-Deficient Core, Joule **3**, 1140 (2019).
[16] F. Lin, K. Jiang, W. Kaminsky, Z. L. Zhu, and A. K. Y. Jen, A Non-fullerene Acceptor with Enhanced Intermolecular pi-Core Interaction for High-Performance Organic Solar Cells, J. Am. Chem. Soc. **142**, 15246 (2020).
[17] Y. B. Lin, Y. Firdaus, F. H. Isikgor, M. I. Nugraha, E. Yengel, G. T. Harrison, R. Hallani, A. El-Labban, H. Faber, C. Ma, X. P. Zheng, A. Subbiah, C. T. Howells, O. M. Bakr, I. McCulloch, S. De Wolf, L. Tsetseris, and T. D. Anthopoulos, Self-Assembled Monolayer Enables Hole Transport Layer-Free Organic Solar Cells with 18% Efficiency and Improved Operational Stability, ACS Energy Lett. **5**, 2935 (2020).
[18] Q. S. Liu, Y. F. Jiang, K. Jin, J. Q. Qin, J. G. Xu, W. T. Li, J. Xiong, J. F. Liu, Z. Xiao, K. Sun, S. F. Yang, X. T. Zhang, and L. M. Ding, 18% Efficiency organic solar cells, Sci Bull **65**, 272 (2020).
[19] J. H. Hou, O. Inganas, R. H. Friend, and F. Gao, Organic solar cells based on non-fullerene acceptors, Nat. Mater. **17**, 119 (2018).
[20] S. S. Chen, Y. M. Wang, L. Zhang, J. B. Zhao, Y. Z. Chen, D. L. Zhu, H. T. Yao, G. Y. Zhang, W. Ma, R. H. Friend, P. C. Y. Chow, F. Gao, and H. Yan, Efficient Nonfullerene Organic Solar Cells with Small Driving Forces for Both Hole and Electron Transfer, Adv. Mater. **30**, 1804215 (2018).
[21] X. Y. Zhu, Q. Yang, and M. Muntwiler, Charge-Transfer Excitons at Organic Semiconductor Surfaces and Interfaces, Acc. Chem. Res. **42**, 1779 (2009).
[22] H. Bassler and A. Kohler, "Hot or cold": how do charge transfer states at the donor-acceptor interface of an organic solar cell dissociate?, PCCP **17**, 28451 (2015).
[23] D. Fazzi, M. Barbatti, and W. Thiel, Hot and Cold Charge-Transfer Mechanisms in Organic Photovoltaics: Insights into the Excited States of Donor/Acceptor Interfaces, J. Phys. Chem. Lett. **8**, 4727 (2017).
[24] G. Grancini, M. Maiuri, D. Fazzi, A. Petrozza, H. J. Egelhaaf, D. Brida, G. Cerullo, and G. Lanzani, Hot exciton dissociation in polymer solar cells, Nat. Mater. **12**, 29 (2013).
[25] A. E. Jailaubekov, A. P. Willard, J. R. Tritsch, W. L. Chan, N. Sai, R. Gearba, L. G. Kaake, K. J. Williams, K. Leung, P. J. Rossky, and X. Y. Zhu, Hot charge-transfer excitons set the time limit for charge separation at donor/acceptor interfaces in organic photovoltaics, Nat. Mater. **12**, 66 (2013).

[26] B. M. Savoie, A. Rao, A. A. Bakulin, S. Gelinas, B. Movaghar, R. H. Friend, T. J. Marks, and M. A. Ratner, Unequal Partnership: Asymmetric Roles of Polymeric Donor and Fullerene Acceptor in Generating Free Charge, J. Am. Chem. Soc. **136**, 2876 (2014).
[27] S. Gelinas, A. Rao, A. Kumar, S. L. Smith, A. W. Chin, J. Clark, T. S. van der Poll, G. C. Bazan, and R. H. Friend, Ultrafast Long-Range Charge Separation in Organic Semiconductor Photovoltaic Diodes, Science **343**, 512 (2014).
[28] A. Devizis, J. De Jonghe-Risse, R. Hany, F. Nuesch, S. Jenatsch, V. Gulbinas, and J. E. Moser, Dissociation of Charge Transfer States and Carrier Separation in Bilayer Organic Solar Cells: A Time-Resolved Electroabsorption Spectroscopy Study, J. Am. Chem. Soc. **137**, 8192 (2015).
[29] R. D. Pensack, C. H. Guo, K. Vakhshouri, E. D. Gomez, and J. B. Asbury, Influence of Acceptor Structure on Barriers to Charge Separation in Organic Photovoltaic Materials, J. Phys. Chem. C **116**, 4824 (2012).
[30] A. J. Barker, K. Chen, and J. M. Hodgkiss, Distance Distributions of Photogenerated Charge Pairs in Organic Photovoltaic Cells, J. Am. Chem. Soc. **136**, 12018 (2014).
[31] D. P. Qian, Z. L. Zheng, H. F. Yao, W. Tress, T. R. Hopper, S. L. Chen, S. S. Li, J. Liu, S. S. Chen, J. B. Zhang, X. K. Liu, B. W. Gao, L. Q. Ouyang, Y. Z. Jin, G. Pozina, I. A. Buyanova, W. M. Chen, O. Inganas, V. Coropceanu, J. L. Bredas, H. Yan, J. H. Hou, F. L. Zhang, A. A. Bakulin, and F. Gao, Design rules for minimizing voltage losses in high-efficiency organic solar cells, Nat. Mater. **17**, 703 (2018).
[32] S. D. Dimitrov, M. Azzouzi, J. Wu, J. Yao, Y. Dong, P. S. Tuladhar, B. C. Schroeder, E. R. Bittner, I. McCulloch, J. Nelson, and J. R. Durrant, Spectroscopic Investigation of the Effect of Microstructure and Energetic Offset on the Nature of Interfacial Charge Transfer States in Polymer: Fullerene Blends, J. Am. Chem. Soc. **141**, 4634 (2019).
[33] B. Kattel, L. Qin, T. R. Kafle, and W. L. Chan, Graphene Field-Effect Transistor as a High-Throughput Platform to Probe Charge Separation at Donor-Acceptor Interfaces, J. Phys. Chem. Lett. **9**, 1633 (2018).
[34] S. M. Menke, A. Cheminal, P. Conaghan, N. A. Ran, N. C. Greehnam, G. C. Bazan, T. Q. Nguyen, A. Rao, and R. H. Friend, Order enables efficient electron-hole separation at an organic heterojunction with a small energy loss, Nat. Commun. **9**, 277 (2018).
[35] Y. Liu, L. J. Zuo, X. L. Shi, A. K. Y. Jen, and D. S. Ginger, Unexpectedly Slow Yet Efficient Picosecond to Nanosecond Photoinduced Hole-Transfer Occurs in a Polymer/Nonfullerene Acceptor Organic Photovoltaic Blend, ACS Energy Lett. **3**, 2396 (2018).
[36] T. R. Kafle, B. Kattel, S. Wanigasekara, T. Wang, and W. L. Chan, Spontaneous Exciton Dissociation at Organic Semiconductor Interfaces Facilitated by the Orientation of the Delocalized Electron-Hole Wavefunction, Adv Energy Mater **10**, 1904013 (2020).
[37] L. Perdigon-Toro, H. T. Zhang, A. S. Markina, J. Yuan, S. M. Hosseini, C. M. Wolff, G. Z. Zuo, M. Stolterfoht, Y. P. Zou, F. Gao, D. Andrienko, S. Shoaee, and D. Neher, Barrierless Free Charge Generation in the High-Performance PM6:Y6 Bulk Heterojunction Non-Fullerene Solar Cell, Adv. Mater. **32**, 1906763 (2020).
[38] T. R. Kafle, B. Kattel, T. Wang, and W.-L. Chan, The relationship between the coherent size, binding energy and dissociation dynamics of charge transfer excitons at organic interfaces, J. Phys.: Condens. Matter **30**, 454001 (2018).
[39] T. Wang, T. R. Kafle, B. Kattel, and W.-L. Chan, A Multidimensional View of Charge Transfer Excitons at Organic Donor–Acceptor Interfaces, J. Am. Chem. Soc. **139**, 4098 (2017).

[40] J. Lee, K. Vandewal, S. R. Yost, M. E. Bahlke, L. Goris, M. A. Baldo, J. V. Manca, and T. Van Voorhis, Charge Transfer State Versus Hot Exciton Dissociation in Polymer-Fullerene Blended Solar Cells, J. Am. Chem. Soc. **132**, 11878 (2010).
[41] T. G. J. van der Hofstad, D. Di Nuzzo, M. van den Berg, R. A. J. Janssen, and S. C. J. Meskers, Influence of Photon Excess Energy on Charge Carrier Dynamics in a Polymer-Fullerene Solar Cell, Adv Energy Mater **2**, 1095 (2012).
[42] K. Vandewal, S. Albrecht, E. T. Hoke, K. R. Graham, J. Widmer, J. D. Douglas, M. Schubert, W. R. Mateker, J. T. Bloking, G. F. Burkhard, A. Sellinger, J. M. J. Frechet, A. Amassian, M. K. Riede, M. D. McGehee, D. Neher, and A. Salleo, Efficient charge generation by relaxed charge-transfer states at organic interfaces, Nat. Mater. **13**, 63 (2014).
[43] G. C. Zhang, X. K. Chen, J. Y. Xiao, P. C. Y. Chow, M. R. Ren, G. Kupgan, X. C. Jiao, C. C. S. Chan, X. Y. Du, R. X. Xia, Z. M. Chen, J. Yuan, Y. Q. Zhang, S. F. Zhang, Y. D. Liu, Y. P. Zou, H. Yan, K. S. Wong, V. Coropceanu, N. Li, C. J. Brabec, J. L. Bredas, H. L. Yip, and Y. Cao, Delocalization of exciton and electron wavefunction in non-fullerene acceptor molecules enables efficient organic solar cells, Nat. Commun. **11**, 3943 (2020).
[44] W. G. Zhu, A. P. Spencer, S. Mukherjee, J. M. Alzola, V. K. Sangwan, S. H. Amsterdam, S. M. Swick, L. O. Jones, M. C. Heiber, A. A. Herzing, G. P. Li, C. L. Stern, D. M. DeLongchamp, K. L. Kohlstedt, M. C. Hersam, G. C. Schatz, M. R. Wasielewski, L. X. Chen, A. Facchetti, and T. J. Marks, Crystallography, Morphology, Electronic Structure, and Transport in Non-Fullerene/Non-Indacenodithienothiophene Polymer:Y6 Solar Cells, J. Am. Chem. Soc. **142**, 14532 (2020).
[45] M. Causa, J. De Jonghe-Risse, M. Scarongella, J. C. Brauer, E. Buchaca-Domingo, J. E. Moser, N. Stingelin, and N. Banerji, The fate of electron-hole pairs in polymer: fullerene blends for organic photovoltaics, Nat. Commun. **7**, 12556 (2016).
[46] J. A. Bartelt, Z. M. Beiley, E. T. Hoke, W. R. Mateker, J. D. Douglas, B. A. Collins, J. R. Tumbleston, K. R. Graham, A. Amassian, H. Ade, J. M. J. Frechet, M. F. Toney, and M. D. McGehee, The Importance of Fullerene Percolation in the Mixed Regions of Polymer-Fullerene Bulk Heterojunction Solar Cells, Adv Energy Mater **3**, 364 (2013).
[47] W. Chen, T. Xu, F. He, W. Wang, C. Wang, J. Strzalka, Y. Liu, J. G. Wen, D. J. Miller, J. H. Chen, K. L. Hong, L. P. Yu, and S. B. Darling, Hierarchical Nanomorphologies Promote Exciton Dissociation in Polymer/Fullerene Bulk Heterojunction Solar Cells, Nano Lett. **11**, 3707 (2011).
[48] F. C. Jamieson, E. B. Domingo, T. McCarthy-Ward, M. Heeney, N. Stingelin, and J. R. Durrant, Fullerene crystallisation as a key driver of charge separation in polymer/fullerene bulk heterojunction solar cells, Chem Sci **3**, 485 (2012).
[49] T. Wang, T. R. Kafle, B. Kattel, Q. Liu, J. Wu, and W.-L. Chan, Growing Ultra-flat Organic Films on Graphene with a Face-on Stacking via Moderate Molecule-Substrate Interaction, Scientific Reports **6** (2016).
[50] T. Wang, T. R. Kafle, B. Kattel, and W. L. Chan, Observation of an Ultrafast Exciton Hopping Channel in Organic Semiconducting Crystals, J. Phys. Chem. C **120**, 7491 (2016).
[51] S. R. Forrest, Ultrathin organic films grown by organic molecular beam deposition and related techniques, Chem. Rev. **97**, 1793 (1997).
[52] W. Chen, S. Chen, H. Huang, D. C. Qi, X. Y. Gao, and A. T. S. Wee, Molecular orientation dependent interfacial dipole at the F16CuPc/CuPc organic heterojunction interface, Appl. Phys. Lett. **92**, 063308 (2008).

[53] T. Nonaka, T. Date, S. Tomita, N. Nagai, M. Nishimura, Y. Murata, and A. Ishitani, Phthalocyanines Ultrathin Alternating Layer Film on Silicon, Prepared by Molecular-Beam Deposition, Thin Solid Films **237**, 87 (1994).

[54] T. Wang, Q. F. Liu, C. Caraiani, Y. P. Zhang, J. Wu, and W. L. Chan, Effect of Interlayer Coupling on Ultrafast Charge Transfer from Semiconducting Molecules to Mono- and Bilayer Graphene, Phys. Rev. Appl. **4**, 014016 (2015).

[55] T. Wang and W. L. Chan, Dynamical Localization Limiting the Coherent Transport Range of Excitons in Organic Crystals, J. Phys. Chem. Lett. **5**, 1812 (2014).

[56] T. Wang, T. R. Kafle, B. Kattel, Q. F. Liu, J. Wu, and W. L. Chan, Growing Ultra-flat Organic Films on Graphene with a Face-on Stacking via Moderate Molecule-Substrate Interaction, Sci. Rep. **6**, 28895 (2016).

[57] G. Witte and C. Woll, Growth of aromatic molecules on solid substrates for applications in organic electronics, J. Mater. Res. **19**, 1889 (2004).

[58] M. Schwarze, W. Tress, B. Beyer, F. Gao, R. Scholz, C. Poelking, K. Ortstein, A. A. Gunther, D. Kasemann, D. Andrienko, and K. Leo, Band structure engineering in organic semiconductors, Science **352**, 1446 (2016).

[59] W. Chen, H. Huang, S. Chen, Y. L. Huang, X. Y. Gao, and A. T. S. Wee, Molecular orientation-dependent ionization potential of organic thin films, Chemistry of Materials **20**, 7017 (2008).

[60] S. Duhm, G. Heimel, I. Salzmann, H. Glowatzki, R. L. Johnson, A. Vollmer, J. P. Rabe, and N. Koch, Orientation-dependent ionization energies and interface dipoles in ordered molecular assemblies, Nat Mater **7**, 326 (2008).

[61] See Supplemental Material at [URL will be inserted by publisher] for the supporting spectra.

[62] M. Schwarze, K. S. Schellhammer, K. Ortstein, J. Benduhn, C. Gaul, A. Hinderhofer, L. P. Toro, R. Scholz, J. Kublitski, S. Roland, M. Lau, C. Poelking, D. Andrienko, G. Cuniberti, F. Schreiber, D. Neher, K. Vandewal, F. Ortmann, and K. Leo, Impact of molecular quadrupole moments on the energy levels at organic heterojunctions, Nat. Commun. **10**, 2466 (2019).

[63] W. Chen, D. C. Qi, Y. L. Huang, H. Huang, Y. Z. Wang, S. Chen, X. Y. Gao, and A. T. S. Wee, Molecular orientation dependent energy level alignment at organic− organic heterojunction interfaces, The Journal of Physical Chemistry C **113**, 12832 (2009).

[64] M. Oehzelt, K. Akaike, N. Koch, and G. Heimel, Energy-level alignment at organic heterointerfaces, Sci. Adv. **1**, 1501127 (2015).

[65] G. M. Bancroft, R. P. Gupta, A. H. Hardin, and M. Ternan, Quantitative Electron-Spectroscopy for Chemical-Analyses of Bitumen Processing Catalysts, Anal. Chem. **51**, 2102 (1979).

[66] Y. Ozawa, Y. Nakayama, S. Machida, H. Kinjo, and H. Ishii, Maximum probing depth of low-energy photoelectrons in an amorphous organic semiconductor film, J. Electron. Spectrosc. Relat. Phenom. **197**, 17 (2014).

[67] L. Graf, K. Ortstein, L. P. Doctor, M. Naumann, J. Beyer, J. Heitmann, K. Leo, and M. Knupfer, New charge-transfer states in blends of ZnPC with F8ZnPC, AIP Adv. **11**, 025230 (2021).

[68] P. K. Watkins, A. B. Walker, and G. L. B. Verschoor, Dynamical Monte Carlo modelling of organic solar cells: The dependence of internal quantum efficiency on morphology, Nano Lett. **5**, 1814 (2005).

[69] T. R. Kafle, T. Wang, B. Kattel, Q. Liu, Y. Gong, J. Wu, and W.-L. Chan, Hot Exciton Relaxation and Exciton Trapping in Single-Walled Carbon Nanotube Thin Films, J. Phys. Chem. C **120**, 24482 (2016).

[70] L. Miaja-Avila, J. R. Tritsch, A. Wolcott, W. L. Chan, C. A. Nelson, and X. Y. Zhu, Direct Mapping of Hot-Electron Relaxation and Multiplication Dynamics in PbSe Quantum Dots, Nano Lett. **12**, 1588 (2012).

[71] W. L. Chan, M. Ligges, A. Jailaubekov, L. Kaake, L. Miaja-Avila, and X. Y. Zhu, Observing the Multiexciton State in Singlet Fission and Ensuing Ultrafast Multielectron Transfer, Science **334**, 1541 (2011).

[72] T. R. Kafle, B. Kattel, P. Yao, P. Zereshki, H. Zhao, and W. L. Chan, Effect of the Interfacial Energy Landscape on Photoinduced Charge Generation at the ZnPc/MoS2 Interface, J. Am. Chem. Soc. **141**, 11328 (2019).

[73] Y. Yao, X. Y. Xie, and H. B. Ma, Ultrafast Long-Range Charge Separation in Organic Photovoltaics: Promotion by Off-Diagonal Vibronic Couplings and Entropy Increase, J. Phys. Chem. Lett. **7**, 4830 (2016).

[74] N. R. Monahan, K. W. Williams, B. Kumar, C. Nuckolls, and X. Y. Zhu, Direct Observation of Entropy-Driven Electron-Hole Pair Separation at an Organic Semiconductor Interface, Phys. Rev. Lett. **114**, 247003 (2015).

[75] B. A. Gregg, Entropy of Charge Separation in Organic Photovoltaic Cells: The Benefit of Higher Dimensionality, J. Phys. Chem. Lett. **2**, 3013 (2011).

[76] S. N. Hood and I. Kassal, Entropy and Disorder Enable Charge Separation in Organic Solar Cells, J. Phys. Chem. Lett. **7**, 4495 (2016).

[77] A. A. Kocherzhenko, D. Lee, M. A. Forsuelo, and K. B. Whaley, Coherent and Incoherent Contributions to Charge Separation in Multichromophore Systems, J. Phys. Chem. C **119**, 7590 (2015).

[78] H. Vazquez and A. Troisi, Calculation of rates of exciton dissociation into hot charge-transfer states in model organic photovoltaic interfaces, Phys. Rev. B **88**, 205304 (2013).

[79] G. Giovannetti, G. Brocks, and J. van den Brink, Ab initio electronic structure and correlations in pristine and potassium-doped molecular crystals of copper phthalocyanine, Phys. Rev. B **77**, 035133 (2008).

[80] S. Saito and A. Oshiyama, Cohesive Mechanism and Energy-Bands of Solid C60, Phys. Rev. Lett. **66**, 2637 (1991).

[81] H. Jiang, J. Ye, P. Hu, F. X. Wei, K. Z. Du, N. Wang, T. Ba, S. L. Feng, and C. Kloc, Fluorination of Metal Phthalocyanines: Single-Crystal Growth, Efficient N-Channel Organic Field-Effect Transistors, and Structure-Property Relationships, Sci. Rep. **4**, 7573 (2014).

[82] J. E. Norton and J. L. Bredas, Theoretical characterization of titanyl phthalocyanine as a p-type organic semiconductor: Short intermolecular pi-pi interactions yield large electronic couplings and hole transport bandwidths, J. Chem. Phys. **128**, 034701 (2008).

[83] F. Iwatsu, T. Kobayashi, and N. Uyeda, Solvent Effects on Crystal-Growth and Transformation of Zinc Phthalocyanine, J. Phys. Chem. **84**, 3223 (1980).

[84] X. Liu, Y. X. Li, K. Ding, and S. Forrest, Energy Loss in Organic Photovoltaics: Nonfullerene Versus Fullerene Acceptors, Phys. Rev. Appl. **11**, 024060 (2019).